

Topological superconductivity in superconducting chiral topological semimetals with parallel spin-momentum locking

Yingyi Huang^{1,2}

¹*School of Physics and Optoelectronic Engineering,
Guangdong University of Technology, Guangzhou 510006, China*

²*Guangdong Provincial Key Laboratory of Sensing Physics and System Integration Applications,
Guangdong University of Technology, Guangzhou, 510006, China*

(Dated: August 2, 2024)

Distinguished from conventional band-inversion-induced Weyl semimetals, chiral topological semimetals host helicoid-arc surface states originating from time-reversal invariant momenta of the Brillouin zone. Motivated by the experimental observation of parallel spin-momentum locking in chiral topological semimetals, we find that parallel spin-momentum locking leads to helicoid-arc surface states. We also investigate the potential intrinsic topological phases in a superconducting chiral topological semimetal with s_{\pm} -wave pairing. We find that a first-order time-reversal invariant topological superconductor can host one Majorana cone for closed Fermi surfaces. Interestingly, there are two Majorana cones when the Fermi surfaces become open. In addition, a second-order topological superconductor with chiral Majorana states can be realized in the presence of a mixture of s_{\pm} - and id -wave pairing. We show that chiral topological semimetals are fascinating platforms for exploring intrinsic unconventional superconductivity and topological superconductivity.

I. INTRODUCTION

Topological superconductors (TSCs) hosting Majorana zero modes have been actively pursued for its important role in fault-tolerant quantum computation [1–7]. The higher-order counterpart of TSC, which manifests as localized modes at $(d - m)$ -dimensional boundaries in a d -dimensional material is also an area of intense investigation [8–26]. However, only a limited number of realistic models have been proposed in intrinsic materials. Very recently, superconductivity have been observed in chiral topological semimetals [27, 28], it has been considered an ideal platform for conventional TSC [29–32]. However, the study of higher-order TSC in chiral topological semimetal is still lacking.

The chiral topological semimetal, realized on crystals free of chirality-inverting symmetries, have attracted a lot of attention for their host of topological nontrivial fermions [33–39]. These topological fermions including Kramers-Weyl fermion or multifold fermion locates at time-reversal invariant momenta (TRIM) with single or multiple band degeneracy [40–42], depending on crystal symmetries. Distinguished from conventional band-inversion-induced Weyl semimetal, chiral semimetal hosts large topological non-trivial energy window, which leads to helicoid-arc surface states and features intriguing optoelectronic and spintronic properties [35, 43–46].

These topological properties of chiral topological semimetals arise from its unique spin-orbit coupling, which leads to parallel spin-momentum locking (SML) [47, 48]. Although both the surface state of Weyl semimetals and chiral topological semimetals show Dirac-cone-like energy nodes, chiral topological semimetals exhibit a parallel SML spin texture on spin-split Fermi sur-

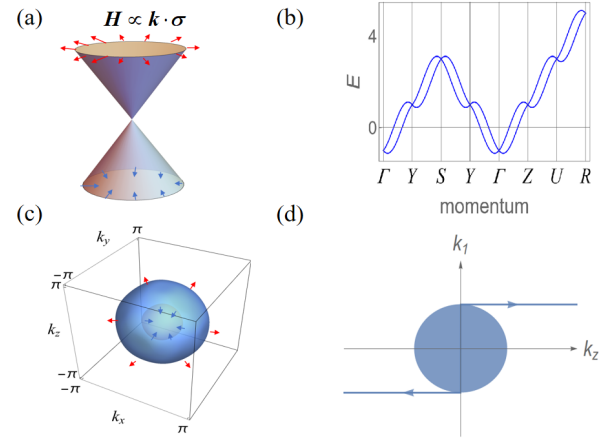


FIG. 1. (Color online)(a)The dispersion of the surface state with parallel SML in a chiral topological semimetal. (b) The band structure for the SG 16 tight-binding model (Eq. 1) in the presence of parallel SML. The parallel SML splits the two-fold band degeneracy everywhere except at the TRIMs. (c) Spin-texture of the two spherical Fermi surfaces. (d) Schematics of the helicoid-arc surface states attached the projection of Fermi surface.

faces (FSs) [48, 49], as shown in Fig. 1(a). This winding spin-texture of chiral topological semimetal carries a topological charge. Unconventional superconducting states have been found in non-centrosymmetric superconductors with antisymmetric spin-orbit coupling [50]. How the parallel SML in chiral topological semimetals acts on spin-triplet cooper pairing remains to be investigated.

In this work, we address these questions in the context of a single orbital model with parallel SML. The paper is organized as follows. In Sec. II, the topologi-

cal properties of chiral topological semimetal and Weyl semimetal are compared, and parallel SML is used to explain the appearance of the helicoid-arc surface state. In Sec. III, the superconducting pairings are introduced. In Sec. IV, we show that the model with parallel SML can realize first-order time-reversal invariant TSCs in the presence of $s\pm$ -wave SC pairing. Remarkably, by turning the Fermi surface structure, we find two TSC phases with topological number $\nu = 1$ and 2 respectively. In Sec. V, we show two second-order TSC phases when the id -wave is present. A further discussion and conclusion are presented in Sec. IV.

II. 3D METAL WITH PARALLEL SPIN-MOMENTUM LOCKING

While most chiral topological semimetals found in experiments host multiple degenerate band touching points, we can use a single degenerate band model to illustrate the physics [47]. We consider a three-dimensional (3D) metal with a single orbital in space group No. 16 described by the Hamiltonian $\hat{H}_0 = \sum_{\mathbf{k}} c_{\mathbf{k}}^\dagger \mathcal{H}_0(\mathbf{k}) c_{\mathbf{k}}$, where

$$\mathcal{H}_0(\mathbf{k}) = \varepsilon(\mathbf{k})\sigma_0 + \alpha \sum_{i=x,y,z} \sin k_i \sigma_i. \quad (1)$$

Here, $\varepsilon(\mathbf{k}) = -t(\cos k_x + \cos k_y + \cos k_z) - \mu$ is the kinetic energy term and α represents the strength of parallel SML. σ_i are Pauli matrices in the spin basis. Note that in the weak spin-momentum coupling limit, σ represents the true electron spin. This is distinct from the orbital pseudo-spin degree of freedom in other topological materials. In this basis, the kinetic energy $\varepsilon(\mathbf{k})$ term is with the same sign in (\uparrow, \downarrow) basis.

The topological features of chiral topological semimetal are distinct from those of Weyl semimetal and other topological matters. The first difference can be seen from its lack of band inversion mechanism. While the band inversion mechanism is first proposed to topological semimetals protected by inversion symmetry, it also applies to semimetals protected by time-reversal symmetry [51, 52]. In the following, we discuss the latter ones. We expand the Hamiltonian around Γ point ($k_x, k_y, k_z = (0, 0, 0)$) as

$$\mathcal{H}_0(k_x, k_y, k_z) = \varepsilon_0(\mathbf{k}) + \sum_{i=1}^3 \alpha_i(\mathbf{k})\sigma_i \quad (2)$$

with $\varepsilon_0(\mathbf{k}) = -3t + 3t(k_x^2 + k_y^2 + k_z^2)/2 - \mu$ and $\alpha_i(\mathbf{k}) = \alpha k_i$ for $i = x, y, z$. In contrast, in conventional Weyl semimetal, the third term in the summation should be in the form $\alpha_z(\mathbf{k}) = m - \frac{1}{2}k_x^2 - \frac{1}{2}k_y^2$ with m being mass.

There are three Pauli matrices anticommuting with each other in chiral topological semimetal. This leads to a band gap closing at Γ point when the three conditions

$\alpha_i(\mathbf{k}) = 0$ are satisfied. This is similar to Weyl nodes, the band crossing point in conventional Weyl semimetals. However, a chiral topological semimetal has linear energy dispersions in all three directions, while a band-inverted Weyl semimetal has a quadratic energy dispersion in the k_z direction. Since only the quadratic direction is the direction for two gap-closing points to dissociate, quadratic energy dispersion is a necessary condition for band inversion. As a result, the absence of a quadratic term in the Hamiltonian of chiral topological semimetal makes it different from Weyl semimetals.

The second difference is in the spin texture of Fermi surfaces. The spin-orbit coupling splits the spin degeneracy of bands in each k point in the Brillouin zone except at TRIM, as shown in Fig. 1(b). Depending on the chemical potential μ , this induces two time-reversal-symmetric spin-split Fermi surfaces as shown in Fig. 1(c). We can calculate the spin expectation of the higher-energy band with the formula $s_i = \langle \psi^j | \sigma_i | \psi^j \rangle$ and determine the spin texture, where ψ^j denotes the eigenvector. Intriguingly, the strength of spin polarization is momentum-independent and the direction is along the normal vector of the Fermi surface. This spin texture has been observed by spin- and angle-resolved photoemission spectroscopy measurements [48]. The spin polarization s_i gives a non-trivial Chern number $\mathcal{C} = 1$, corresponding to electronic topological chirality [47]. Recent angle-resolved photoemission spectroscopy (ARPES) experiment has observed helicoid-arc surface states in CoSi and RhSi [35], which spirals around high-symmetry momenta. While the existence of surface states is linked to electronic topological chirality by bulk-edge correspondence, an explanation of the helicoid behavior is absent. In the following, we will show that the helicoid behavior naturally arises from parallel SML.

To derive the low-energy Hamiltonian for the surface states, we first do a coordinates transformation $\mathbf{a}_1 = \frac{\hat{x}-\hat{y}}{\sqrt{2}}$, $\mathbf{a}_2 = \frac{\hat{x}+\hat{y}}{\sqrt{2}}$ and $\mathbf{a}_3 = \hat{z}$. Without loss of generality, we focus on the $x_2 = 0$ surface. Following a standard approach, we expand the lattice Hamiltonian around Γ and then find the corresponding low-energy surface Hamiltonian takes the form [53]

$$H_s(k_1, k_z) = \begin{cases} -\alpha k_z - \mu + t(k^2), & \text{when } k_1 > 0 \\ \alpha k_z - \mu + t(k^2), & \text{when } k_1 < 0. \end{cases} \quad (3)$$

Here, $t(k^2) = -t + \frac{1}{2}tk_1^2 + \frac{1}{2}tk_2^2$.

Let us first consider the $t = 0$ case. The solution of the surface Hamiltonian $\psi(z) = e^{-ik_z z}$ for positive k_1 is a chiral propagating mode in the negative z -direction of energy $E = \alpha k_z - \mu$. The solution of the surface Hamiltonian $\psi(z) = e^{ik_z z}$ for negative k_1 is a chiral propagating mode in the positive z -direction of energy $E = \alpha k_z - \mu$. The normal state has Fermi arcs at $k_z = \mp\mu/\alpha$ where μ/α corresponds to the maximum radius of the FS in the $k_1 - k_z$ plane. The Fermi arc tangentially connects

with the projection of FS in the surface BZ [54]. Now we turn to the $t \neq 0$ case. When $k_1 > 0$, the surface state propagates in the negative k_z direction of energy $E = \alpha k_z + t(k_z^2)$. In contrast, when $t_1 < 0$, the surface state propagates in the opposite direction of energy $E = \alpha k_z - t(k_z^2)$ and extends diagonally across the surface BZ. This helical arc is a result of the parallel SML αk_z term, which is absent in other topological materials.

We can see that although it does not determine the existence of topological surface states, the αk_z term plays an important role in the dispersion of the topological surface states. In the following, we will show that αk_z term also affects the behavior of superconducting surface states.

III. SUPERCONDUCTING PAIRING

Superconductivity has been found in RhGe and BeAu [28, 55–58], whose electronic structure is akin to chiral topological semimetals in nonsymmorphic space group No. 198. Although in the presence of SML, both odd-parity and even-parity pairings can coexist, we only consider even-pairing for simplicity since two opposite momentums on the Fermi surface carry opposite spin polarizations.

The superconducting order parameter can be written in the explicit form

$$\Delta(\mathbf{k}) = \Delta_0 + \Delta_s \eta_s(\mathbf{k}) + i\Delta_d \eta_d(\mathbf{k}), \quad (4)$$

where Δ_0 , Δ_s and $i\Delta_d$ represent onsite s -, extended s - and id -wave SC respectively. $\Delta_s(\mathbf{k}) = \Delta_s \eta_s(\mathbf{k})$ with $\eta_s(\mathbf{k}) = \sum_{i=x,y,z} \cos k_i$ and $\Delta_d(\mathbf{k}) = \Delta_d \eta_d(\mathbf{k})$ with $\eta_d(\mathbf{k}) = \cos k_x - \cos k_y$.

On the Nambu basis $\Psi_{\mathbf{k}}^T = (c_{\mathbf{k}\uparrow}, c_{\mathbf{k}\downarrow}, -c_{-\mathbf{k}\downarrow}^\dagger, c_{-\mathbf{k}\uparrow}^\dagger)$, the Bogoliubov-de Gennes (BdG) Hamiltonian is $H_{\text{BdG}} = \frac{1}{2} \sum_{\mathbf{k}} \Psi_{\mathbf{k}}^\dagger \mathcal{H}_{\text{BdG}}(\mathbf{k}) \Psi_{\mathbf{k}}$, where

$$\mathcal{H}_{\text{BdG}}(\mathbf{k}) = \varepsilon(\mathbf{k})\tau_z\sigma_0 + \alpha\tau_z(\sin k_x\sigma_x + \sin k_y\sigma_y + \sin k_z\sigma_z) - \Delta_s(\mathbf{k})\tau_x - \Delta_d(\mathbf{k})\tau_y. \quad (5)$$

Here, the Pauli matrices τ_i and σ_i act on the particle-hole and spin degrees of freedom respectively.

This model satisfies the particle-hole symmetry $\Xi \mathcal{H}_{\text{BdG}}(\mathbf{k}) \Xi^{-1} = -\mathcal{H}_{\text{BdG}}(-\mathbf{k})$ with the operator $\Xi = \tau_y \sigma_y \mathcal{K}$. Importantly, while the normal part and the s -wave pairing part of the Hamiltonian respect time-reversal symmetry (TRS)

$$\mathcal{T} \mathcal{H}_{\text{BdG}}(-\mathbf{k}) \mathcal{T} = \mathcal{H}_{\text{BdG}}(\mathbf{k}) \quad (6)$$

associated with the operator $\mathcal{T} = i\tau_0 \sigma_y \mathcal{K}$, the id -wave pairing breaks TRS.

In addition, the model hosts two-fold rotational symmetries along principle axes x , y , and z . This allows the appearance of a second-order TSC phase, which relies on the anisotropic of a system.

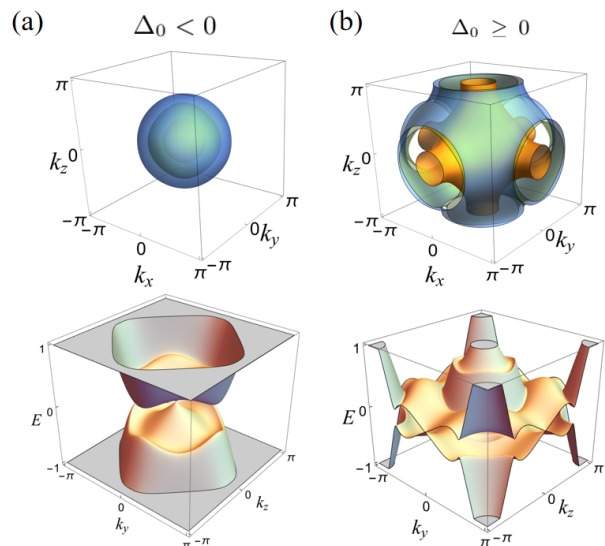


FIG. 2. First-order TSC phases. Upper panels: The representative configurations of two Fermi surfaces (in blue and yellow colors) of the single-particle bands and pairing nodes surface (in green color). Lower panel: BdG spectrum of a slab geometry with open-boundary condition only along the x direction. We choose parameter values $t = 1$, $\alpha = 0.6$, $\Delta_s = 1$. (a) For closed FS, $\Delta_0 = -1.8$ and $\mu = -2$; (b) for open FS, $\Delta_0 = 0.1$, $\mu = -0.3$.

IV. FIRST-ORDER TSC

The time-reversal invariant superconductors in 3D are mathematically classified by an integer invariant \mathbb{Z} [59]. They are different from TSC in 2D, which is classified by a \mathbb{Z}_2 . Most importantly, this allows the appearance of a TSC phase with a large topological number. It has been demonstrated that an odd parity pairing gapped superconductor is a first-order TSC if the Fermi surface encloses an odd number of TRIMs in the Brillouin zone [60]. Accordingly, we should investigate the relative position of FS configuration and SC pairing nodes. In this section, we will consider a momentum-dependent s_{\pm} gap function pairing, which is the most symmetric one.

In our system, after basis transformation [61], the BdG Hamiltonian can be decoupled into two independent parts $\mathcal{H}(\mathbf{k}) = \mathcal{H}_+(\mathbf{k}) \oplus \mathcal{H}_-(\mathbf{k})$

$$\mathcal{H}_{\pm}(\mathbf{k}) = \begin{pmatrix} |\varepsilon(\mathbf{k})| \pm \alpha(\mathbf{k}) & \Delta_{\pm}(\mathbf{k}) \\ \Delta_{\pm}^*(\mathbf{k}) & -|\varepsilon(\mathbf{k})| \mp \alpha(\mathbf{k}) \end{pmatrix}, \quad (7)$$

where $\Delta_{\pm}(\mathbf{k}) = \frac{(\Delta_0 + \Delta_s \eta_s(\mathbf{k}))(\sin k_x \pm i \sin k_y)}{\sqrt{\sin^2 k_x + \sin^2 k_y}}$ and $\alpha(\mathbf{k}) = \alpha \sqrt{\sin^2 k_x + \sin^2 k_y + \sin^2 k_z}$.

In the presence of SML, the number of normal state FSs is determined by the energy spectra of $\mathcal{H}_-(\mathbf{k})$, since the energy spectra $\mathcal{H}_+(\mathbf{k})$ are always gapped. The FS number must be even due to the time-reversal symmetry.

In particular, when $|\varepsilon(\mathbf{k})| - \alpha(\mathbf{k}) = 0$ have solutions, we can see that the normal state of a superconductor has two FSs. Although the $\alpha(\mathbf{k})$ has a different form from the general 2D model with Rashba and Dresselhaus spin-orbit couplings [24], it only changes the shape of Fermi surfaces.

The main feature of the FSs in this system is that they can be closed or open surfaces in 3D, determined by the amplitude of chemical potential μ . This is different from the Fermi circles induced by the Rashba spin-orbit coupling as $|\varepsilon(\mathbf{k})| = \alpha\sqrt{\sin^2 k_x + \sin^2 k_y}$, which are always closed. Most interestingly, the pairing nodal surface (PNS) of $\Delta_s(\mathbf{k}) = 0$, can always be chosen to separate two regions in which Δ_s has opposite signs. Indeed, according to $\cos k_x + \cos k_y + \cos k_z = -\Delta_0/\Delta_s$, the PNS in 3D satisfied can be closed or open surfaces, determined by the sign of Δ_0 .

Now we first look at the case with closed FS. When $\Delta_0 \ll 0$, a closed PNS is located between two disconnected FS, as shown in Fig. 2(a). The corresponding surface state of BdG Hamiltonian exhibits a Majorana cone at $(k_y, k_z) = (0, 0)$ point, as can be seen in Fig. 2(a). Actually, according to the bulk-edge correspondence, the number of Majorana cones corresponds to the winding number. For the closed surface, we can use a formula in the weak-pairing limit [62]

$$\nu = \frac{1}{2} \sum_i \text{sgn}(\Delta_i) C_i, \quad (8)$$

where $\text{sgn}(\Delta_i)$ denotes the sign of pairing on the i th FS and C_i denotes the first Chern number. The signs of pairing on the two FS are opposite, characterizing a first-order TSC phase with $\nu = 1$.

The most interesting case is the 3D FSs in the open shape in the first BZ. It is in contrast to the 2D FS centered at the corner of FS, which is in a close form. Now we consider a situation for $\Delta_0 \geq 0$ as shown in Fig. 2(b). We can see that two open FSs are separated by an open PNS without any crossings. The appearance of open FSs is a natural result of a spin-orbit coupling with three components, which splits FS in three dimensions.

Since the FS is no longer a closed surface, we can not use Eq. 8. However, we can look at the topology in a space of projectors. A projection operator of occupied state is defined as $P_{\mathbf{k}} = \sum_{n \in \text{filled}} |u_{n\mathbf{k}}\rangle \langle u_{n\mathbf{k}}|$ with $|u_{n\mathbf{k}}\rangle$ being the n -th Bloch wave function at \mathbf{k} . In the presence of chiral symmetry, it can be further brought into an off-diagonal form $Q_{\mathbf{k}} = 1 - 2P_{\mathbf{k}}$. The winding number can be written as [63]

$$\nu = \frac{1}{24\pi^2} \int d^3\mathbf{k} \epsilon^{ijk} \text{Tr} \left[Q_{\mathbf{k}}^\dagger \partial_i Q_{\mathbf{k}} Q_{\mathbf{k}}^\dagger \partial_j Q_{\mathbf{k}} Q_{\mathbf{k}}^\dagger \partial_k Q_{\mathbf{k}} \right]. \quad (9)$$

In the TSC phase with open FSs and PNS, we find a winding number of $\nu = -2$. The corresponding surface

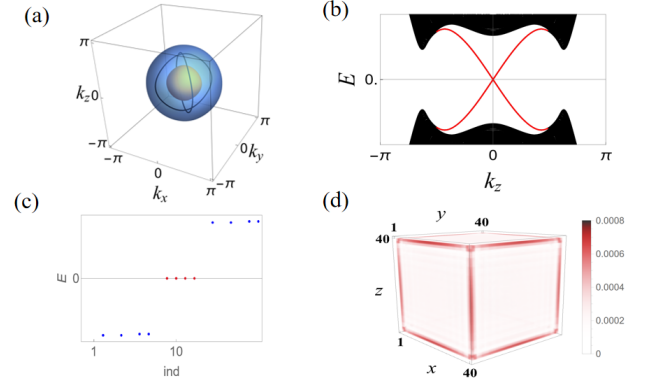


FIG. 3. Second-order TSC phase for closed FSs. (a) The configuration of FS and removable Dirac pairing nodes (black lines fulfill $\Delta_0 + \Delta_s \eta_s = 0$ and $\Delta_d \eta_d = 0$). (b) Chiral Majorana hinge mode along z direction. Both x and y directions have open-boundary conditions with $N_x = N_y = 50$ lattice sites. (c) The eigenvalues of the BdG Hamiltonian around zero energy. (d) The probability density profiles of four Majorana hinge states. Both three directions have open-boundary conditions with $N_x = N_y = N_z = 40$ lattice sites. The parameters are the same as Fig. 1(a) except $\Delta_d = 0.5$.

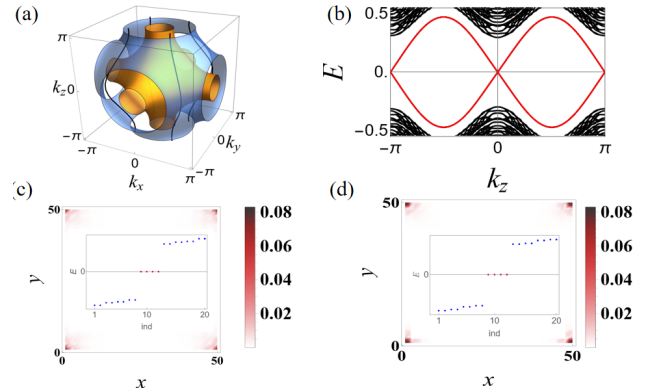


FIG. 4. Second-order TSC phase for open FSs. (a) The configuration of FS and removable Dirac pairing nodes (black lines fulfill $\Delta_0 + \Delta_s \eta_s = 0$ and $\Delta_d \eta_d = 0$.) (b) Chiral Majorana hinge mode along z direction. Both x and y directions have open-boundary conditions with $N_x = N_y = 50$ lattice sites. (c,d) The probability density profiles of four Majorana hinge states and the eigenvalues of the BdG Hamiltonian around zero energy (red points of the inset) at (c) $k_z = 0$ and (d) $k_z = \pi$. The parameters are the same as Fig. 1(b) except $\Delta_d = 0.5$.

state of BdG Hamiltonian exhibits two Majorana surface cones at $(k_y, k_z) = (\pi, 0)$ and $(k_y, k_z) = (0, \pi)$ points. This $\nu = -2$ phase is absent in systems with Rashba and Dresselhaus spin-orbit coupling, which have only two components.

V. SECOND-ORDER TSC

Although the pairing nature in RhGe and BeAu is still under investigation, multigap superconductivity is recently reported [27, 57, 58]. Thus we consider a mixture of s - and id - wave SC pairing, in which the d -wave SC breaks the time-reversal symmetry.

According to the symmetry classification [59], the 3D superconductor without time-reversal symmetry is in class D. The first-order TSC phase becomes trivial and the helical edge states are gapped out due to the breaking of time-reversal symmetry. However, d -wave SC order has line nodes along the direction $k_x = \pm k_y$. Analogous to the 2D case [14, 24], we can expect a second-order TSC phase.

Now for the closed FS case, the PNS becomes lines simultaneously fulfilled $\Delta_0 + \Delta_s \eta_s = 0$ and $\Delta_d \eta_d = 0$, as shown in Fig. 3(a). When open boundary condition is used in both x and y directions, we can see chiral Majorana hinge modes along the z direction in Fig. 3(b). At $k_z = 0$, the four eigenstates in the middle of the BdG energy spectrum have zero energies, confirming the break of time-reversal symmetry in Fig. 3(c). The localization of the Majorana modes on all the hinges is shown by the density distribution of the lowest four eigenstates in Fig. 3(d), confirming the system is in a second-order TSC.

Now we turn to the FSs with open shape in Fig. 4(a). In the first-order TSC phase without id -wave SC, we have found two Dirac cones on (100) surface, crossing at $(k_y, k_z) = (0, \pi)$ and $(k_y, k_z) = (\pi, 0)$ respectively. When the id -wave SC is turned on, we can expect the pairing gaps of the Dirac cones to have sign reversal at two momenta simultaneously. Figure 4(b) shows that two pairs of chiral Majorana hinge modes cross at $k_z = 0$ and $k_z = \pi$ in the energy spectrum of cylinder sample with open boundary condition in x and y directions. Interestingly, these edge states are isolated from the bulk bands. The spatial profile of the eigenvalues near zero energy confirms the localization of the Majorana hinge modes for $k_z = 0$ and $k_z = \pi$ in Fig. 4(c) and (d) respectively.

VI. DISCUSSION AND CONCLUSION

In this work, we showed that both first- and second-order TSC phases can emerge in a model with parallel SML. We found that the parallel SML not only leads to helicoid-like arc surface states, but also gives rises to interesting features in Majorana surface states. In particular, a first-order TSC phase with $\nu = -2$ for open FSs has no 2D analog. Also, a second-order TSC phase for open FSs has chiral Majorana hinge modes crossing at two momenta.

The parallel spin-momentum locking has a decisive impact on the topological superconductivity in chiral topo-

logical semimetals. In the above calculations, we use a single orbital model in a symmorphic space group 16 to show the existence of TSC phases. However, our results can be expected to be generalized to nonsymmorphic chiral crystal materials, especially RhGe and AuBe in space group 198 which exhibits superconductivity [28, 55–58]. In Ref. 49, 64, and 65, first principle calculation and group theory analysis found symmetry-preserved monopole-like spin texture at the Γ point in CoSi, a material in space group 198. Actually, tight-binding model calculation and mean-field analysis have shown the existence of first-order TSC phase in chiral topological semimetal with s_{\pm} SC pairing [29].

Our study extends the topological superconductivity beyond the Rashba spin-orbit coupling physics. In the past decades, the connection between Rashba spin-orbit coupling and Dirac physics in topological materials has been well studied. The spin-momentum locking is admitted as a central ingredient giving rise to remarkable topological properties. However, in recent years, condensed matter physics has found new spin polarization behaviors in Fermi surfaces. For example, in recent studies, the spin texture of the collinear and noncollinear altermagnetism have been linked to topological superconductivity [66]. We expect the novel spin-momentum locking in Fermi surfaces could give rise to a variety of exotic physics in TSC.

ACKNOWLEDGMENTS

We would like to thank Zhongbo Yan for helpful discussions. This work is supported by the National Natural Science Foundation of China (Grant No. 12104099 and No. 12274095) and Guangzhou Science and Technology Program (Grant No. 2024A04J0272)

-
- [1] N. Read and D. Green, Paired states of fermions in two dimensions with breaking of parity and time-reversal symmetries and the fractional quantum hall effect, *Physical Review B* **61**, 10267 (2000).
 - [2] A. Y. Kitaev, Unpaired majorana fermions in quantum wires, *Physics-uspekhi* **44**, 131 (2001).
 - [3] J. Alicea, New directions in the pursuit of majorana fermions in solid state systems, *Reports on progress in physics* **75**, 076501 (2012).
 - [4] C. Beenakker, Search for majorana fermions in superconductors, *Annual Review of Condensed Matter Physics* **4**, 113 (2013).
 - [5] S. R. Elliott and M. Franz, *Colloquium* : Majorana fermions in nuclear, particle, and solid-state physics, *Rev. Mod. Phys.* **87**, 137 (2015).
 - [6] M. Sato and Y. Ando, Topological superconductors: a review, *Reports on Progress in Physics* **80**, 076501 (2017).

- [7] T. D. Stanescu and S. Tewari, Majorana fermions in semiconductor nanowires: fundamentals, modeling, and experiment, *Journal of Physics: Condensed Matter* **25**, 233201 (2013).
- [8] J. Langbehn, Y. Peng, L. Trifunovic, F. von Oppen, and P. W. Brouwer, Reflection-symmetric second-order topological insulators and superconductors, *Physical review letters* **119**, 246401 (2017).
- [9] E. Khalaf, Higher-order topological insulators and superconductors protected by inversion symmetry, *Physical Review B* **97**, 205136 (2018).
- [10] M. Geier, L. Trifunovic, M. Hoskam, and P. W. Brouwer, Second-order topological insulators and superconductors with an order-two crystalline symmetry, *Physical Review B* **97**, 205135 (2018).
- [11] X. Zhu, Tunable majorana corner states in a two-dimensional second-order topological superconductor induced by magnetic fields, *Physical Review B* **97**, 205134 (2018).
- [12] Z. Yan, F. Song, and Z. Wang, Majorana corner modes in a high-temperature platform, *Physical review letters* **121**, 096803 (2018).
- [13] Q. Wang, C.-C. Liu, Y.-M. Lu, and F. Zhang, High-temperature majorana corner states, *Physical review letters* **121**, 186801 (2018).
- [14] Y. Wang, M. Lin, and T. L. Hughes, Weak-pairing higher order topological superconductors, *Physical Review B* **98**, 165144 (2018).
- [15] Z. Yan, Higher-order topological odd-parity superconductors, *Physical review letters* **123**, 177001 (2019).
- [16] T. Liu, J. J. He, F. Nori, *et al.*, Majorana corner states in a two-dimensional magnetic topological insulator on a high-temperature superconductor, *Physical Review B* **98**, 245413 (2018).
- [17] R.-X. Zhang, W. S. Cole, X. Wu, and S. D. Sarma, Higher-order topology and nodal topological superconductivity in fe (se, te) heterostructures, *Physical review letters* **123**, 167001 (2019).
- [18] X.-H. Pan, K.-J. Yang, L. Chen, G. Xu, C.-X. Liu, and X. Liu, Lattice-symmetry-assisted second-order topological superconductors and majorana patterns, *Physical review letters* **123**, 156801 (2019).
- [19] X. Zhu, Second-order topological superconductors with mixed pairing, *Physical Review Letters* **122**, 236401 (2019).
- [20] Y.-T. Hsu, W. S. Cole, R.-X. Zhang, and J. D. Sau, Inversion-protected higher-order topological superconductivity in monolayer wte 2, *Physical Review Letters* **125**, 097001 (2020).
- [21] Z. Wu, Z. Yan, and W. Huang, Higher-order topological superconductivity: Possible realization in fermi gases and sr 2 ruo 4, *Physical Review B* **99**, 020508 (2019).
- [22] Y. Volpez, D. Loss, and J. Klinovaja, Second-order topological superconductivity in π -junction rashba layers, *Physical review letters* **122**, 126402 (2019).
- [23] Y.-J. Wu, J. Hou, Y.-M. Li, X.-W. Luo, X. Shi, and C. Zhang, In-plane zeeman-field-induced majorana corner and hinge modes in an s-wave superconductor heterostructure, *Physical Review Letters* **124**, 227001 (2020).
- [24] M. Kheirkhah, Z. Yan, Y. Nagai, and F. Marsiglio, First-and second-order topological superconductivity and temperature-driven topological phase transitions in the extended hubbard model with spin-orbit coupling, *Physical Review Letters* **125**, 017001 (2020).
- [25] S. Qin, C. Fang, F.-C. Zhang, and J. Hu, Topological superconductivity in an extended s-wave superconductor and its implication to iron-based superconductors, *Physical Review X* **12**, 011030 (2022).
- [26] X. Wu, W. A. Benalcazar, Y. Li, R. Thomale, C.-X. Liu, and J. Hu, Boundary-obstructed topological high-t c superconductivity in iron pnictides, *Physical Review X* **10**, 041014 (2020).
- [27] A. Tsvyashchenko, V. Sidorov, A. Petrova, L. Fomicheva, I. Zibrov, and V. Dmitrienko, Superconductivity and magnetism in noncentrosymmetric rhge, *Journal of Alloys and Compounds* **686**, 431 (2016).
- [28] D. Salamatina, A. Tsvyashchenko, A. Salamatina, A. Velichkov, M. Magnitskaya, N. Chitchev, V. Sidorov, L. Fomicheva, M. Mikhin, M. Kozin, *et al.*, Hyperfine field studies of the high-pressure phase of non-centrosymmetric superconductor rhge (b20) doped with hafnium, *Journal of Alloys and Compounds* **850**, 156601 (2021).
- [29] Y. Huang and S.-K. Jian, Three-dimensional time reversal invariant topological superconductivity in doped chiral topological semimetals, *Physical Review B* **103**, L161113 (2021).
- [30] C. Lee, C. Yoon, T. Kim, S. B. Chung, and H. Min, Topological multiband s-wave superconductivity in coupled multifold fermions, *Physical Review B* **104**, L241115 (2021).
- [31] S. Mardanya, M. Kargarian, R. Verma, T.-R. Chang, S. Chowdhury, H. Lin, A. Bansil, A. Agarwal, and B. Singh, Unconventional superconducting pairing in a b20 kramers weyl semimetal, *arXiv preprint arXiv:2309.05880* (2023).
- [32] Z. S. Gao, X.-J. Gao, W.-Y. He, X. Y. Xu, T. Ng, and K. Law, Topological superconductivity in multifold fermion metals, *Quantum Frontiers* **1**, 3 (2022).
- [33] Z. Rao, H. Li, T. Zhang, S. Tian, C. Li, B. Fu, C. Tang, L. Wang, Z. Li, W. Fan, *et al.*, Observation of unconventional chiral fermions with long fermi arcs in cosi, *Nature* **567**, 496 (2019).
- [34] D. Takane, Z. Wang, S. Souma, K. Nakayama, T. Nakamura, H. Oinuma, Y. Nakata, H. Iwasawa, C. Cacho, T. Kim, *et al.*, Observation of chiral fermions with a large topological charge and associated fermi-arc surface states in cosi, *Physical review letters* **122**, 076402 (2019).
- [35] D. S. Sanchez, I. Belopolski, T. A. Cochran, X. Xu, J.-X. Yin, G. Chang, W. Xie, K. Manna, V. Süß, C.-Y. Huang, *et al.*, Topological chiral crystals with helicoidal quantum states, *Nature* **567**, 500 (2019).
- [36] N. B. Schröter, D. Pei, M. G. Vergniory, Y. Sun, K. Manna, F. De Juan, J. A. Krieger, V. Süß, M. Schmidt, P. Dudin, *et al.*, Chiral topological semimetal with multifold band crossings and long fermi arcs, *Nature Physics* **15**, 759 (2019).
- [37] B. Q. Lv, Z.-L. Feng, J.-Z. Zhao, N. F. Q. Yuan, A. Zong, K. F. Luo, R. Yu, Y.-B. Huang, V. N. Strocov, A. Chikina, *et al.*, Observation of multiple types of topological fermions in pdbise, *Physical Review B* **99**, 241104(R) (2019).
- [38] M. Yao, K. Manna, Q. Yang, A. Fedorov, V. Voroshnin, B. V. Schwarze, J. Hornung, S. Chattopadhyay, Z. Sun, S. N. Guin, *et al.*, Observation of giant spin-split fermi-arc with maximal chern number in the chiral topological semimetal ptga, *Nature Communications* **11**, 2033

- (2020).
- [39] N. B. Schröter, S. Stolz, K. Manna, F. De Juan, M. G. Vergniory, J. A. Krieger, D. Pei, T. Schmitt, P. Dudin, T. K. Kim, et al., Observation and control of maximal chern numbers in a chiral topological semimetal, *Science* **369**, 179 (2020).
- [40] B. Bradlyn, J. Cano, Z. Wang, M. Vergniory, C. Felser, R. J. Cava, and B. A. Bernevig, Beyond dirac and weyl fermions: Unconventional quasiparticles in conventional crystals, *Science* **353**, aaf5037 (2016).
- [41] G. Chang, S.-Y. Xu, B. J. Wieder, D. S. Sanchez, S.-M. Huang, I. Belopolski, T.-R. Chang, S. Zhang, A. Bansil, H. Lin, et al., Unconventional chiral fermions and large topological fermi arcs in rhsi, *Phys. Rev. Lett.* **119**, 206401 (2017).
- [42] P. Tang, Q. Zhou, and S.-C. Zhang, Multiple types of topological fermions in transition metal silicides, *Physical review letters* **119**, 206402 (2017).
- [43] D. Rees, K. Manna, B. Lu, T. Morimoto, H. Borrmann, C. Felser, J. Moore, D. H. Torchinsky, and J. Orenstein, Helicity-dependent photocurrents in the chiral weyl semimetal rhsi, *Science advances* **6**, eaba0509 (2020).
- [44] D. Dutta, B. Ghosh, B. Singh, H. Lin, A. Politano, A. Bansil, and A. Agarwal, Collective plasmonic modes in the chiral multifold fermionic material cosi, *Physical Review B* **105**, 165104 (2022).
- [45] T.-Y. Hsieh, B. B. Prasad, and G.-Y. Guo, Helicity-tunable spin hall and spin nernst effects in unconventional chiral fermion semimetals x y ($x = \text{co, rh}$; $y = \text{si, ge}$), *Physical Review B* **106**, 165102 (2022).
- [46] Z. Ni, K. Wang, Y. Zhang, O. Pozo, B. Xu, X. Han, K. Manna, J. Paglione, C. Felser, A. G. Grushin, et al., Giant topological longitudinal circular photo-galvanic effect in the chiral multifold semimetal cosi, *Nature communications* **12**, 154 (2021).
- [47] G. Chang, B. J. Wieder, F. Schindler, D. S. Sanchez, I. Belopolski, S.-M. Huang, B. Singh, D. Wu, T.-R. Chang, T. Neupert, et al., Topological quantum properties of chiral crystals, *Nature materials* **17**, 978 (2018).
- [48] J. A. Krieger, S. Stolz, I. Robredo, K. Manna, E. C. McFarlane, M. Date, B. Pal, J. Yang, E. B. Guedes, J. H. Dil, et al., Weyl spin-momentum locking in a chiral topological semimetal, *Nature communications* **15**, 3720 (2024).
- [49] M. Lin, I. Robredo, N. B. Schröter, C. Felser, M. G. Vergniory, and B. Bradlyn, Spin-momentum locking from topological quantum chemistry: Applications to multifold fermions, *Physical Review B* **106**, 245101 (2022).
- [50] M. Smidman, M. Salamon, H. Yuan, and D. Agterberg, Superconductivity and spin-orbit coupling in non-centrosymmetric materials: a review, *Reports on Progress in Physics* **80**, 036501 (2017).
- [51] N. Armitage, E. Mele, and A. Vishwanath, Weyl and dirac semimetals in three-dimensional solids, *Reviews of Modern Physics* **90**, 015001 (2018).
- [52] S. Murakami and S.-i. Kuga, Universal phase diagrams for the quantum spin hall systems, *Physical Review B—Condensed Matter and Materials Physics* **78**, 165313 (2008).
- [53] See Sec. I of the supplemental material for effective odd-parity superconductivity model.
- [54] F. Haldane, Attachment of surface” fermi arcs” to the bulk fermi surface:” fermi-level plumbing” in topological metals, arXiv preprint arXiv:1401.0529 (2014).
- [55] B. Matthias, Superconductivity of aube, *Journal of Physics and Chemistry of Solids* **10**, 342 (1959).
- [56] D. J. Rebar, S. M. Birnbaum, J. Singleton, M. Khan, J. C. Ball, P. W. Adams, J. Y. Chan, D. P. Young, D. A. Browne, and J. F. DiTusa, Fermi surface, possible unconventional fermions, and unusually robust resistive critical fields in the chiral-structured superconductor aube, *Physical Review B* **99**, 094517 (2019).
- [57] R. Khasanov, R. Gupta, D. Das, A. Amon, A. Leithe-Jasper, and E. Svanidze, Multiple-gap response of type-i noncentrosymmetric beau superconductor, *Physical Review Research* **2**, 023142 (2020).
- [58] R. Khasanov, R. Gupta, D. Das, A. Leithe-Jasper, and E. Svanidze, Single-gap versus two-gap scenario: Specific heat and thermodynamic critical field of the non-centrosymmetric superconductor beau, *Physical Review B* **102**, 014514 (2020).
- [59] C.-K. Chiu, J. C. Y. Teo, A. P. Schnyder, and S. Ryu, Classification of topological quantum matter with symmetries, *Rev. Mod. Phys.* **88**, 035005 (2016).
- [60] L. Fu and E. Berg, Odd-parity topological superconductors: theory and application to $\text{Cu}_x\text{Bi}_2\text{Se}_3$, *Physical review letters* **105**, 097001 (2010).
- [61] See Sec. II of the supplemental material for the surface theory.
- [62] X.-L. Qi, T. L. Hughes, and S.-C. Zhang, Topological invariants for the fermi surface of a time-reversal-invariant superconductor, *Physical Review B* **81**, 134508 (2010).
- [63] A. P. Schnyder, S. Ryu, A. Furusaki, and A. W. W. Ludwig, Classification of topological insulators and superconductors in three spatial dimensions, *Physical Review B* **78**, 195125 (2008).
- [64] W. Tan, X. Jiang, Y. Li, X. Wu, J. Wang, and B. Huang, A unified understanding of diverse spin textures of kramers–weyl fermions in nonmagnetic chiral crystals, *Advanced Functional Materials* **32**, 2208023 (2022).
- [65] D. Gosálbez-Martínez, A. Crepaldi, and O. V. Yazyev, Diversity of radial spin textures in chiral materials, *Physical Review B* **108**, L201114 (2023).
- [66] S. H. Lee, Y. Qian, and B.-J. Yang, Fermi surface spin texture and topological superconductivity in spin-orbit free noncollinear antiferromagnets, *Physical Review Letters* **132**, 196602 (2024).
- [67] J. Alicea, Majorana fermions in a tunable semiconductor device, *Physical Review B* **81**, 125318 (2010).

Supplemental Material

I. THE SURFACE THEORY

To derive a low energy Hamiltonian, a quadratic term of k is needed. We do a transform $k_1 = \frac{k_x - k_y}{\sqrt{2}}$ and $k_2 = \frac{k_x + k_y}{\sqrt{2}}$. Thus, we define a set of new basis vectors $\mathbf{a}_1 = \frac{\hat{x} - \hat{y}}{\sqrt{2}}$, $\mathbf{a}_2 = \frac{\hat{x} + \hat{y}}{\sqrt{2}}$ and $\mathbf{a}_3 = \hat{z}$ and introduce a new set of Pauli matrices $\sigma_1 = \sigma_x - \sigma_y$ and $\sigma_2 = \sigma_x + \sigma_y$. In the new basis, the Hamiltonian becomes

$$\mathcal{H}(\mathbf{k}) = -t(2 \cos \frac{k_1}{\sqrt{2}} \cos \frac{k_2}{\sqrt{2}} + \cos k_z) - \mu + \alpha \left(\sin \frac{k_1}{\sqrt{2}} \cos \frac{k_2}{\sqrt{2}} \sigma_1 + \cos \frac{k_1}{\sqrt{2}} \sin \frac{k_2}{\sqrt{2}} \sigma_2 + \sin k_z \sigma_z \right) \quad (\text{S-1})$$

where the Pauli matrices σ_i act on the spin degrees of freedom, respectively.

From the low-energy Hamiltonian around $(k_1, k_2, k_z) = (0, 0, 0)$,

$$\mathcal{H}(\mathbf{k}) = (-3t + tk_1^2/2 + tk_2^2/2 + tk_z^2/2 - \mu) + \alpha k_1/\sqrt{2}(1 - k_2^2/4)\sigma_1 + \alpha(1 - k_1^2/4)k_2/\sqrt{2}\sigma_2 + \alpha k_z \sigma_z \quad (\text{S-2})$$

For the surface on the $x_2 = 0$ plane, the sample occupies the whole $x_2 > 0$ region. As the translation symmetry is broken in the x_2 direction, k_2 needs to be replaced by $-i\partial_{x_2}$. The Hamiltonian can be decomposed into two parts, i.e., $H = H_0 + H_p$, with

$$H_0(k_1, -i\partial_{x_2}, k_z) = \frac{1}{\sqrt{2}}\alpha k_1(1 + \frac{1}{4}\partial_{x_2}^2)\sigma_1 - i\frac{1}{\sqrt{2}}\alpha(1 - \frac{1}{4}k_1^2)\partial_{x_2}\sigma_2 + \alpha k_z \sigma_z \quad (\text{S-3})$$

and

$$H_p(k_1, -i\partial_{x_2}, k_z) = -3t + \frac{1}{2}tk_1^2 - \frac{1}{2}t\partial_{x_2}^2 + \frac{1}{2}tk_z^2 - \mu \quad (\text{S-4})$$

The part H_p will be treated as a perturbation.

When solving the wave function for the H_0 satisfies $H_0\psi_\alpha(x_2) = E_\alpha\psi_\alpha(x_2)$, the boundary condition is $\psi_\alpha(0) = \psi_\alpha(\infty) = 0$. Calculation gives two solutions with $E_\alpha = 0$, whose form are

$$\psi(x_2) = \mathcal{N} \sin(\kappa_1 x_2) e^{-\kappa_2 x_2} e^{ik_1 x_1} e^{ik_z z} \chi. \quad (\text{S-5})$$

with the normalization constant $\mathcal{N} = 2\sqrt{\kappa_2(\kappa_1^2 + \kappa_2^2)}/\kappa_1^2$.

Since the parameter κ_2 must be positive, we should discuss in $k_1 > 0$ and $k_1 < 0$ case separately. We first focus on the $k_1 > 0$ regime, where the two parameters κ_1 and κ_2 are given by

$$\kappa_1 = \frac{\sqrt{-k_1^4 + 24k_1^2 - 16}}{2k_1}, \kappa_2 = \frac{4 - k_1^2}{2k_1}. \quad (\text{S-6})$$

The corresponding eigenvectors χ_α satisfies $\sigma_z \chi_\alpha = -\chi_\alpha$. We choose

$$\chi_1 = |\sigma_z = -1\rangle. \quad (\text{S-7})$$

The matrix elements of the perturbation H_p in this basis are $H_s(k_1, k_z) = \int_0^\infty dx_2 \psi_\alpha^*(x_2) H_p(k_1, -i\partial_{x_2}, k_2) \psi_\beta(x_2)$. In particular, we find $\int_0^\infty dx_2 \psi^*(x_2) (\frac{1}{2}t\partial_{x_2}^2) \psi(x_2) = 2t$.

In the basis $(\psi_1, \psi_2)^T$, the surface-state Hamiltonian reads

$$H_{x_2=0}(k_1 > 0, k_z) = -\alpha k_z - \mu + t(k^2), \quad (\text{S-8})$$

$$t(k^2) = -t + \frac{1}{2}tk_1^2 + \frac{1}{2}tk_z^2.$$

If we consider the $k_1 < 0$ regime, the difference is in the κ'_2 given by

$$\kappa'_2 = \frac{4 - k_1^2}{-2k_1}. \quad (\text{S-9})$$

The corresponding wave function is changed to spinors χ'_α satisfy $\sigma_z \chi'_\alpha = \chi'_\alpha$. We choose $\chi'_1 = |\sigma_z = 1\rangle$, in which the surface-state Hamiltonian is

$$H_{x_2=0}(k_1 < 0, k_z) = \alpha k_z - \mu + t(k^2). \quad (\text{S-10})$$

Note that the sign of α is changed with k_1 , which is the characteristic of the helicoid-arc surface state.

II. EFFECTIV ODD-PARITY SUPERCONDUCTIVITY MODEL

The normal state Hamiltonian with parallel spin-momentum coupling is

$$H_0 = \sum_{\mathbf{k}} (c_{\mathbf{k},\uparrow}^\dagger, c_{\mathbf{k},\downarrow}^\dagger) \begin{pmatrix} \xi_{\mathbf{k}} + \alpha_z & \alpha_x - i\alpha_y \\ \alpha_x + i\alpha_y & \xi_{\mathbf{k}} - \alpha_z \end{pmatrix} \begin{pmatrix} c_{\mathbf{k},\uparrow} \\ c_{\mathbf{k},\downarrow} \end{pmatrix}, \quad (\text{S-11})$$

where $\alpha_i = \alpha \sin k_i$ for $i = x, y, z$. Note that $\alpha_z = \alpha \sin k_z$ is different from the out-of-plane Zeeman field, which is used in the basis transformation mapping the spin-orbit coupling and $s + id$ -wave pairing to an effective odd-parity pairing [24] Here, for $k' = -k$, $\alpha_z(-\mathbf{k}) = -\alpha_z(\mathbf{k})$

The even-parity superconductivity(SC) is described by

$$H_{\text{SC}} = \sum_{\mathbf{k}} (\Delta_s(\mathbf{k}) + i\Delta_d(\mathbf{k})) c_{\mathbf{k},\uparrow}^\dagger c_{-\mathbf{k},\downarrow}^\dagger + h.c., \quad (\text{S-12})$$

where $\Delta_s(\mathbf{k}) = \Delta_0 + \Delta_s \eta_s(\mathbf{k})$ and $\Delta_d(\mathbf{k}) = \Delta_d \eta_d(\mathbf{k})$.

The SC part can be rewritten on the Nambu basis as

$$H_{\text{SC}} = \sum_{\mathbf{k}} (c_{\mathbf{k},\uparrow}^\dagger, c_{\mathbf{k},\downarrow}^\dagger) \begin{pmatrix} 0 & -(\Delta_s(\mathbf{k}) + i\Delta_d(\mathbf{k})) \\ (\Delta_s(\mathbf{k}) + i\Delta_d(\mathbf{k})) & 0 \end{pmatrix} \begin{pmatrix} c_{-\mathbf{k},\uparrow}^\dagger \\ c_{-\mathbf{k},\downarrow}^\dagger \end{pmatrix} + h.c. \quad (\text{S-13})$$

Following Ref. [24, 67], we can do the transformation,

$$(c_{\mathbf{k},\uparrow}^\dagger, c_{\mathbf{k},\downarrow}^\dagger) = \begin{pmatrix} \cos \frac{\theta_{\mathbf{k}}}{2} & e^{-i\phi_{\mathbf{k}}} \sin \frac{\theta_{\mathbf{k}}}{2} \\ e^{-i\phi_{\mathbf{k}}} \sin \frac{\theta_{\mathbf{k}}}{2} & -\cos \frac{\theta_{\mathbf{k}}}{2} \end{pmatrix} \begin{pmatrix} c_{\mathbf{k},+}^\dagger \\ c_{\mathbf{k},-}^\dagger \end{pmatrix} + h.c., \quad (\text{S-14})$$

where $\theta_{\mathbf{k}}$ satisfies $\cos \theta_{\mathbf{k}} = \alpha_z / \alpha_{\mathbf{k}}$ with $\alpha_{\mathbf{k}} = \sqrt{\alpha_x^2 + \alpha_y^2 + \alpha_z^2}$ and $\phi_{\mathbf{k}}$ satisfies $e^{i\phi_{\mathbf{k}}} = (\alpha_x + i\alpha_y) / \sqrt{\alpha_x^2 + \alpha_y^2}$. This is different from $\alpha_{\mathbf{k}} = \sqrt{\alpha_x^2 + \alpha_y^2}$ for Rashba spin-orbit coupling [24].

The normal part can be written in a diagonal form

$$H_0 = \sum_{\mathbf{k}} (\varepsilon_{\mathbf{k}} + \alpha) c_{\mathbf{k},+}^\dagger c_{\mathbf{k},+} + (\varepsilon_{\mathbf{k}} - \alpha) c_{\mathbf{k},-}^\dagger c_{\mathbf{k},-}. \quad (\text{S-15})$$

Fortunately, the superconducting part can also be written in a diagonal form

$$H_{\text{SC}} = \frac{1}{2} \sum_{\mathbf{k}} \left(\frac{-(\Delta_s(\mathbf{k}) + i\Delta_d(\mathbf{k}))(\alpha_x + i\alpha_y)}{\sqrt{\alpha_x^2 + \alpha_y^2}} c_{\mathbf{k},+}^\dagger c_{-\mathbf{k},+}^\dagger + h.c. \right) + \frac{1}{2} \sum_{\mathbf{k}} \left(\frac{-(\Delta_s(\mathbf{k}) + i\Delta_d(\mathbf{k}))(\alpha_x - i\alpha_y)}{\sqrt{\alpha_x^2 + \alpha_y^2}} c_{\mathbf{k},-}^\dagger c_{-\mathbf{k},-}^\dagger + h.c. \right). \quad (\text{S-16})$$

The Hamiltonian can be decoupled into two parts, $H = H_+ \oplus H_-$, with

$$H_+ = \sum_{\mathbf{k}} \varepsilon_{\mathbf{k},+} c_{\mathbf{k},+}^\dagger c_{\mathbf{k},+} + \frac{1}{2} \sum_{\mathbf{k}} \left(\frac{(\Delta_s(\mathbf{k}) + i\Delta_d(\mathbf{k}))(\alpha_x + i\alpha_y)}{\sqrt{\alpha_x^2 + \alpha_y^2}} c_{\mathbf{k},+}^\dagger c_{-\mathbf{k},+}^\dagger + h.c. \right), \quad (\text{S-17})$$

$$H_- = \sum_{\mathbf{k}} \varepsilon_{\mathbf{k},-} c_{\mathbf{k},-}^\dagger c_{\mathbf{k},-} + \frac{1}{2} \sum_{\mathbf{k}} \left(\frac{(\Delta_s(\mathbf{k}) + i\Delta_d(\mathbf{k}))(\alpha_x + i\alpha_y)}{\sqrt{\alpha_x^2 - \alpha_y^2}} c_{\mathbf{k},-}^\dagger c_{-\mathbf{k},-}^\dagger + h.c. \right). \quad (\text{S-18})$$